Original Research

Image reconstruction for endoscopic photoacoustic tomography including effects of detector responses

Zheng Sun[1,2] and Huifeng Sun[1,2]

[1]Department of Electronic and Communication Engineering, North China Electric Power University, Baoding 071003, China; [2]Hebei Key Laboratory of Power Internet of Things Technology, North China Electric Power University, Baoding 071003, China
Corresponding author: Zheng Sun. Email: sunzheng@ncepu.edu.cn

Impact Statement

This study offers a promising solution for the issue of image quality degradation in endoscopic photoacoustic tomography caused by detector effects. The proposed model-based scheme involves two steps: establishing the forward imaging model and inversing the forward model through iterative optimization. The imaging model physically describes the light transport, generation of initial pressure, acoustic propagation, and acoustic measurement where the temporal and spatial responses of the detector are incorporated. Our findings have demonstrated improved reconstruction quality by our method compared with conventional back-projection reconstruction and other reconstruction enhancement methods. This study makes a significant contribution to the literature because our approach showed superior performance in improving the quality of endoscopic photoacoustic tomography images.

Abstract

In photoacoustic tomography (PAT), conventional image reconstruction methods are generally based on the assumption of an ideal point-like ultrasonic detector. This assumption is appropriate when the receiving surface of the detector is sufficiently small and/or the distance between the imaged object and the detector is large enough. However, it does not hold in endoscopic applications of PAT. In this study, we propose a model-based image reconstruction method for endoscopic photoacoustic tomography (EPAT), considering the effect of detector responses on image quality. We construct a forward model to physically describe the imaging process of EPAT, including the generation of the initial pressure due to optical absorption and thermoelastic expansion, the propagation of photoacoustic waves in tissues, and the acoustic measurement. The model outputs the theoretical sampling voltage signal, which is the response of the ultrasonic detector to the acoustic pressure reaching its receiving surface. The images representing the distribution map of the optical absorption energy density on cross-sections of the imaged luminal structures are reconstructed from the sampling voltage signals output by the detector through iterative inversion of the forward model. Compared with the conventional approaches based on back-projection and other imaging models, our method improved the quality and spatial resolution of the resulting images.

Keywords: Endoscopic photoacoustic tomography, image reconstruction, detector responses, space impulse response, electric impulse response, model-based image reconstruction

***Experimental Biology and Medicine* 2022; 247: 881–897. DOI: 10.1177/15353702221079570**

Introduction

Photoacoustic tomography (PAT) has been a fast-developing hybrid imaging technique in the past two decades. It can provide high absorption contrast of optical imaging and superior spatial resolution of ultrasonic imaging in deep biological tissues. Reconstructions of high-quality images representing the distribution of optical absorption, initial pressure, and optical parameters of the imaged tissues are essential in PAT. Conventional methods such as analytical methods,[1–5] time reversion (TR),[6] and iterative methods[7–9] enable reconstructions with high quality from complete acoustic measurements. They are generally based on the premise of an ideal point detector with omnidirectional responses (i.e. it is equally sensitive to pressure waves from any direction), ignoring the effects of the detector responses on the acoustic measurements. However, to collect weak PA signals, planar unfocused ultrasonic transducers with large detection areas are usually used in practical applications, considering the drawbacks of the point detector, such as small effective area, poor sensitivity, and low signal-to-noise ratio (SNR). The diffraction effect of flat unfocused transducers affects the acceptance angle and the delay accuracy, resulting in the finite aperture effect.[10,11] In addition, the sampling signal output by the transducers is the result of the convolution of the acoustic pressure reaching the transducer surface with the transducer responses. The responses of the ultrasonic transducers in receive-mode are generally depicted by their spatial impulse response (SIR) and electric impulse response (EIR). EIR characterizes the electrical

Table 1. Comparison of methods for correcting the finite aperture effect in PA imaging.

Method	Advantages	Drawbacks	Applications	
Focused transducers	The tangential resolution is significantly improved.	There is a loss in the radial resolution. The number of geometric focus (*f*) is not considered.	PAT systems with focused transducers which perform 2D circular scanning around large imaging objects such as breast.	
Negative acoustic lens	The tangential resolution is more than three times higher than the flat detector. The larger scanning area can be imaged.	Poor quality of lens leads to signal loss or image artifacts.	PAT systems equipped with an unfocused flat ultrasonic transducer whose surface is completely covered by a negative cylindrical lens.	
Compressed sensing (CS)	The tangential resolution is effectively improved. The artifacts caused by incomplete measurements are eliminated. The system cost and data acquisition time are reduced.	The measuring noises are not considered.	Dirac impulse acoustic sources without considering EIR.	Complete or incomplete PA measurements.
Model-based image reconstruction	The degraded tangential resolution for PAT with finite-sized unfocused transducers is effectively improved, while the radial resolution is reserved. The spatial invariance of resolution is ensured.	A large amount of PA data are required to be collected. High computational burden must be considered due to the iterative optimization.		Complete PA measurements.

PA: photoacoustic; PAT: photoacoustic tomography; EIR: electric impulse response.

response of the transducer. In contrast, SIR models the averaging effect over the active area, reflecting the anisotropic detection sensitivity caused by the finite receiving surface of the transducer.[12] If EIR and SIR are not considered in the image reconstruction algorithms, the image resolution and imaging accuracy will be reduced.

Different methods have been reported to mitigate the impact of detector properties on the quality of PAT images. We classified the main techniques into four categories: focused transducers, negative acoustic lens, compressed sensing (CS), and model-based image reconstruction, as shown in Table 1.

Unlike a point detector, a focused transducer enables detection of the PA radiation generated by the acoustic sources in a specific angle range by its focus, that is, a virtual point detector.[10,13–15] The tangential extension of the point spread functions (PSFs) of a focused transducer is narrower than that of an unfocused transducer, improving the tangential resolution of the reconstructed images. However, this improvement is at the expense of the radial resolution.[13,14] Fortunately, the trade-off between the tangential and radial resolution is acceptable, especially when imaging large objects such as breasts.[14] In addition, the *f*-number of a focused transducer determines its acceptance angle, which also affects the tangential and radial resolution and should be optimized to achieve optimal image reconstruction performance.

A finite-size unfocused detector has a large active area, high sensitivity, good SNR, and a slight acceptance angle. A partial solution is to use a negatively focused acoustic lens attached to the transducer surface to achieve a larger acceptance angle. With such a detector, the tangential resolution can be increased by more than three times than the flat detector.[16–18] In addition, the imaging range can be further improved by enlarging the acceptance angle. However, the quality of lens fabrication, the acoustic reverberation inside the lens, and the film defects between the lens and transducer surface will lead to artifacts in images. In addition, the signal loss caused by acoustic absorption inside the acrylic lens and the impedance mismatch between the acoustically coupled mineral oil and the acrylic lens must also be considered.

CS has been a practical scheme for reconstructing images from incomplete measuring data. It can remove artifacts originating from incomplete measurements while significantly reducing the system cost and data acquisition time. For instance, Chiu *et al*.[19] presented a CS-based method to eliminate the finite aperture effect in PAT image reconstruction by incorporating the SIRs of the finite-sized flat transducer into the linear discrete imaging model. However, they did not consider the impact of noises in the experimental verification.

The model-based scheme has been demonstrated effective in reconstructing images with high quality from complete or incomplete measurements.[20–26] In this scheme, image reconstruction essentially involves the inversion of a forward imaging model. Li and Cheng[27] and Li *et al*.,[28] for the first time, demonstrated the feasibility of model-based reconstruction to solve the problem of the spatial resolution degradation caused by finite-sized unfocused ultrasonic transducers without changing imaging settings. Based on the discrete imaging model, they designed a spatial-temporal optimal filter used for deconvolution with the SIR of the transducer for each point in the PA data set. This method effectively improved the tangential resolution while maintaining the radial resolution. Although it provided uniform peak amplitudes of PSF in all imaging domains, the sidelobe level might become more significant in the case of the object close to the detector surface. Later, various methods for numerically compensating for the transducer effects in image reconstruction algorithms were explored.[12,29–38] These methods are generally computationally burdensome because of their nature of iterative least-squares minimization. However, incorporating far-field approximation into the forward model can reduce the computational complexity.[30]

In addition, deconvolution has been applied to reduce blurring in PA images caused by a finite detector size.[39–45] As a post-processing method for detector data or reconstructed images, the deconvolution-based algorithms can

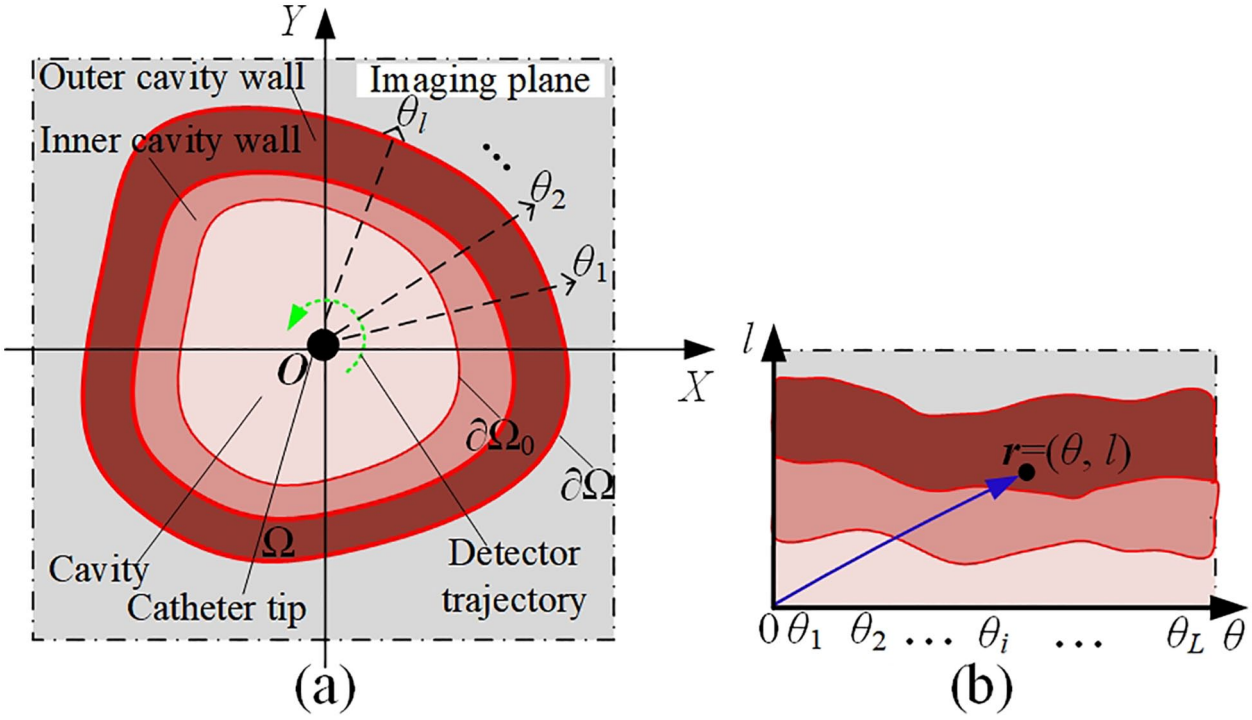

Figure 1. Planar co-ordinate systems of the imaging plane for EPAT. (a) Cartesian co-ordinate system and (b) polar co-ordinate system. (A color version of this figure is available in the online journal.)

improve the image resolution without physically increasing the numerical aperture of the imaging system. However, the possible noises introduced by post-processing procedures should not be neglected.

Recently, Luo *et al.*[46] presented a fast method for correcting the finite aperture effect in circular/spherical-scanning-based PAT systems. The process is based on the quick calculation of SIR-related parameters and compensation of the SIR in the framework of the blood pressure (BP) reconstruction. The simulation and phantom experiments demonstrated improved lateral resolution and SNR over the conventional BP. Luo's method is theoretically more computationally efficient than the model-based scheme. However, they did not consider the EIR of the detector and did not conduct experimental comparisons with the model-based methods.

Note that an essential difficulty with the image reconstruction incorporating the detector effects is the unknown EIR of the transducer. It is usually measured by experiment in practical applications because it is difficult to model it accurately using relatively simple analytical models, and the parameters employed in theoretical models cannot be accurately measured.[20,33] This measurement is very sensitive to noise and other errors, reducing the accuracy of the system matrix.[33,47] The readers are referred to Han *et al.*[33] for a comprehensive survey on the progress of EIR measurement. Alternatively, a joint optimization approach can solve this issue.[36,37] The measured EIR is refined with a variable projection method to recover the optical deposition by exploiting the bi-linearity of the imaging model.[32,33] This approach enables low-cost and adequate compensation for the model mismatch. However, it is required to choose the regularization parameters reasonably to obtain satisfactory reconstruction results.

Endoscopic photoacoustic tomography (EPAT) is an invasive application of PAT for biological luminal structures.[48–51] In this study, we present a model-based image reconstruction method for EPAT, which incorporates the SIR and EIR of the detector into the imaging model. The process involves two steps: establishing a forward imaging model and inversing the forward model through iterative optimization. Results of verification and comparison with conventional BP and other model-based algorithms demonstrate the superiority of our method in improving the quality of EPAT images.

Materials and methods

Forward imaging model incorporating detector responses

EPAT utilizes an imaging catheter with a probe mounted on its tip inserted into the target cavity or lumen. As shown in Figure 1, the transversal imaging plane, that is, the cross-section of the luminal structure, is perpendicular to the catheter located in the image center. The collimating light source is the inward photon flow at the surface boundary facing the source. Light transport in the tissues is modeled by the radiative transfer equation (RTE), which is simplified as a diffusion equation (DE) based on the assumption that the reduced scattering coefficient is much larger than the absorption coefficient.[52] Solving the DE produces light fluence. The optical deposition is proportional to the absorption coefficient and light fluence as follows[53]

$$A(\boldsymbol{r}) = \mu_a(\boldsymbol{r})\Phi(\boldsymbol{r}) \tag{1}$$

where $A(\boldsymbol{r})$, $\mu_a(\boldsymbol{r})$, and $\Phi(\boldsymbol{r})$ denote the absorbed optical energy density (AOED), absorption coefficient, and light

fluence at a location $\boldsymbol{r} \in \Omega$, respectively. Ω is the imaging domain. The initial pressure induced by optical absorption is proportional to the AOED and the Gruneisen coefficient. The acoustic propagation in the tissues is governed by the following PA wave equation[10]

$$\nabla^2 p(\boldsymbol{r},t) - \frac{1}{\left[c_s(\boldsymbol{r})\right]^2} \cdot \frac{\partial^2}{\partial t^2} p(\boldsymbol{r},t) = -A(\boldsymbol{r}) \cdot \frac{\beta_e}{C_P} \cdot \frac{d}{dt} I_e(t) \tag{2}$$

where $p(\boldsymbol{r}, t)$ is the acoustic pressure at location $\boldsymbol{r}$ and time t, C_P is the specific heat capacity at a certain pressure, β_e denotes the thermal expansion coefficient, c_s represents the speed of sound, and $I_e(t)$ is the function depicting the incident laser pulse in time-domain. The initial condition of equation (2) is as follows: $p(\boldsymbol{r},t)|_{t=0} = p_0(\boldsymbol{r})$ and $(\partial / \partial t) p(\boldsymbol{r},t)|_{t=0} = 0$, where $p_0(\boldsymbol{r})$ is the initial pressure.

The photoacoustically induced ultrasonic waves, that is, PA waves, are collected by a finite-sized unfocused ultrasonic transducer in receiving mode along a circular trajectory in the imaging plane. The PA data set collected via a full-view (360°) scanning contains L A-scan lines. The radial angle of the lth A-line is $\theta_l = 360(l-1)/L$, where $l = 1, 2, \ldots, L$. A total of K points are sampled on each A-line. The wave propagation and acquisition are treated as a linear time-invariant system. The voltage signal output by the detector at time t and angle θ_l in response to the acoustic pressure reaching its surface is represented by a $K \times 1$-dimensional vector

$$\boldsymbol{u}_e(\theta_l, t) = \boldsymbol{e}(\theta_l, t) + \int_{r \in \Omega} \boldsymbol{h}_{\mathrm{SIR}}(\theta_l, \boldsymbol{r}, t) * \boldsymbol{h}_e * p(\boldsymbol{r}, t) d\boldsymbol{r} \tag{3}$$

where $\boldsymbol{u}_e(\theta_l, t)$ denotes the theoretical sampling voltage vector at angle θ_l and time t output by the detector, $\boldsymbol{e}(\theta_l, t)$ is the additive measurement noise vector, "*" denotes the convolution in the time-domain, $\boldsymbol{h}_e$ is the EIR vector of the detector, and $\boldsymbol{h}_{\mathrm{SIR}}$ is the SIR vector from the detector position to location $\boldsymbol{r}$[27,28]

$$\boldsymbol{h}_{\mathrm{SIR}}(\theta_l, \boldsymbol{r}, t) = \int_S \frac{1}{2\pi |\boldsymbol{r}_d - \boldsymbol{r}|} \delta\left(t - \frac{\boldsymbol{r}_d - \boldsymbol{r}}{c_s}\right) \cos\theta_l d\boldsymbol{r}_{\mathrm{d}} \tag{4}$$

here, $\boldsymbol{r}_d \in S$ denotes the position on the active area S of the transducer.

Reconstruction of images representing AOED

The spatial distribution of the AOED on a cross-section of the imaged object is reconstructed from the sampling voltage signal output by the detector via inversion of the forward model. The non-linear least square (NLS) problem estimating the AOED at a position $\boldsymbol{r}$ within the imaging domain is defined as follows

$$\hat{A}(\boldsymbol{r}) = \arg\min_{A(\boldsymbol{r})} \left[f(A(\boldsymbol{r})) + g(A(\boldsymbol{r})) \right] \tag{5}$$

where

$$\begin{cases} f(A(\boldsymbol{r})) = \left\| \boldsymbol{u}_m(\boldsymbol{r}) - \boldsymbol{H}(A(\boldsymbol{r})) \right\|^2 \\ g(A(\boldsymbol{r})) = \eta \left\| A(\boldsymbol{r}) \right\|_1 \end{cases} \tag{6}$$

here, $\hat{A}$ denotes the estimated AOED, A represents the AOED to be optimized, $\boldsymbol{u}_m$ is the measured sampling voltage signal, η is the regularization parameter, $g(A(\boldsymbol{r}))$ is the L1 regularization term, $\|\cdot\|$ is the Euclidean norm, and $\boldsymbol{H}(\cdot)$ is the forward imaging operator depicting the process from the AOED to the sampling voltage signal.

The fast iterative shrinkage thresholding algorithm (FISTA)[54] is employed to solve the NLS problem iteratively. The AOED is taken as the unknown being updated at each iteration until the output of the forward model matches the sampling voltage output by the detector. The principle of the FISTA is as follows.

The quadratic approximation of $f(A(\boldsymbol{r}))$ at a given point y is written as

$$\begin{aligned} Q_L(A(\boldsymbol{r}), y) = f(y) + \left\langle A(\boldsymbol{r}) - y, \nabla f(y) \right\rangle \\ + \frac{L}{2} \left\| A(\boldsymbol{r}) - y \right\|^2 + g(A(\boldsymbol{r})) \end{aligned} \tag{7}$$

where $L > 0$ is the Lipschitz constant, ∇f is the gradient of f, and $<\cdot>$ denotes the inner product of two vectors defined by $< \boldsymbol{x}, \boldsymbol{y} >= \boldsymbol{x}^{\mathrm{T}} \boldsymbol{y}$. The minimum of equation (7) is determined as follows

$$p_L(y) = \arg\min_A \left\{ Q_L(A(\boldsymbol{r}), y) \right\} \tag{8}$$

By neglecting the constant terms, equation (8) is rewritten as

$$p_L(y) = \arg\min_A \left\{ \frac{L}{2} \left\| A(\boldsymbol{r}) - \left[y - \frac{1}{L} \nabla f(y) \right] \right\|^2 + g(A(\boldsymbol{r})) \right\} \tag{9}$$

Then, the primary iterative step for solving equation (5) is

$$A_k(\boldsymbol{r}) = p_L(y_k) \tag{10}$$

The detailed steps of iteration are as follows:

Step 1. Initialization. The iteration times $k = 1$; the step size $t_1 = 1$; the initial guess of the AOED is denoted as $A_0(\boldsymbol{r})$; and $y_1 = A_0(\boldsymbol{r})$.

Step 2. Determination of the Lipschitz constant. The Lipschitz constant is determined as follows

$$L = 2\lambda_{\max}\left(\boldsymbol{H}^{\mathrm{T}} \boldsymbol{H}\right) \tag{11}$$

where $\lambda_{\max}(\cdot)$ represents the greatest eigenvalue of a matrix.

Step 3. Calculation of the AOED at the k*th iteration.* The AOED at position $\boldsymbol{r}$ at the kth iteration is determined as follows

$$\begin{aligned} A_k(\boldsymbol{r}) &= p_L(y_k) \\ &= \arg\min_A \left\{ \frac{L}{2} \left\| A(\boldsymbol{r}) - \left(y_k - \frac{1}{L} \nabla f(y_k) \right) \right\|^2 + \eta \left\| A(\boldsymbol{r}) \right\|_1 \right\} \end{aligned} \tag{12}$$

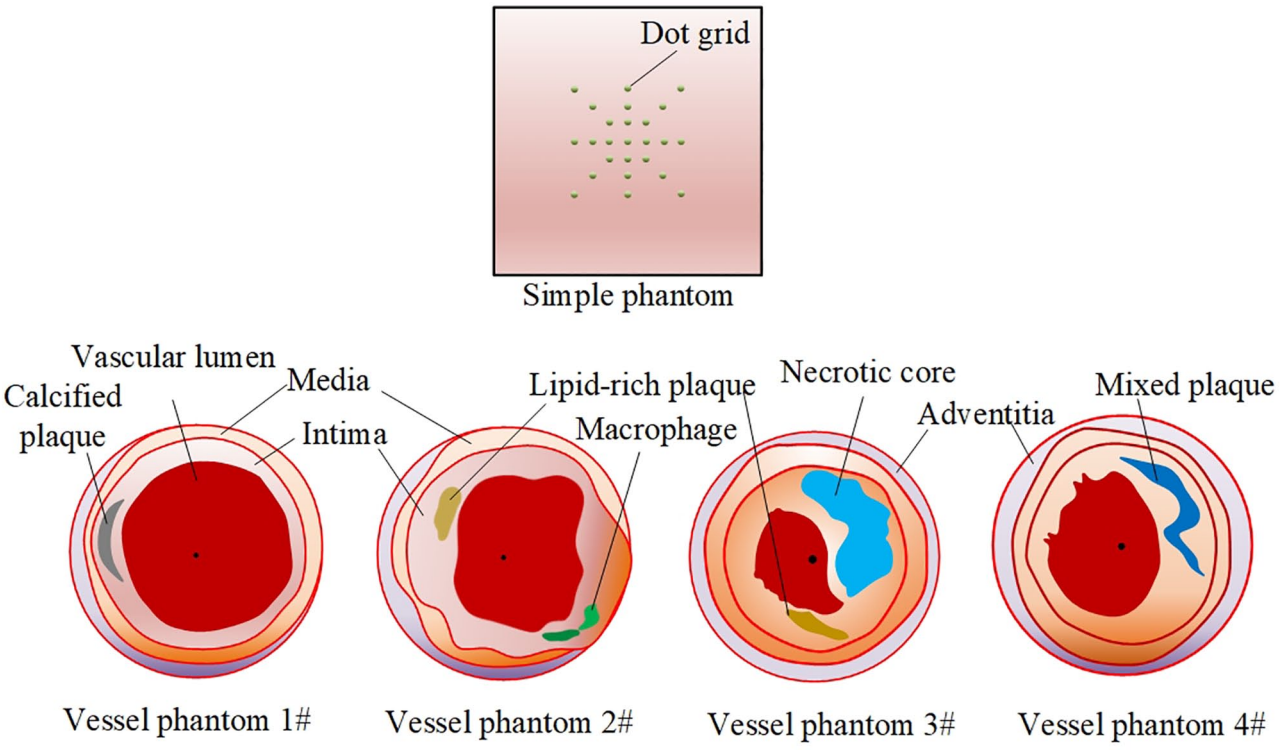

Figure 2. Geometry of simple dot-grid phantom and cross-sections of coronary vessel phantoms. (A color version of this figure is available in the online journal.)

where

$$f(y_k) = \left\| \boldsymbol{u}_m(\boldsymbol{r}) - \boldsymbol{H}(y_k) \right\|^2 \tag{13}$$

and $\boldsymbol{H}(y_k) = \boldsymbol{u}_k(\boldsymbol{r})$ is the theoretical voltage signal output by the detector at the kth iteration.

Step 4. Updating of y_k. y_k and t_k are updated as

$$y_{k+1} = A_k(\boldsymbol{r}) + \frac{t_k - 1}{t_{k+1}} \left[A_k(\boldsymbol{r}) - A_{k-1}(\boldsymbol{r}) \right] \tag{14}$$

and

$$t_{k+1} = \frac{1 + \sqrt{1 + 4t_k^2}}{2} \tag{15}$$

Step 5. Termination of the iteration. The termination of the iteration is determined by

$$\varepsilon = \left\| \boldsymbol{u}_m(\boldsymbol{r}) - \boldsymbol{u}_k(\boldsymbol{r}) \right\|_2^2 \tag{16}$$

where $\varepsilon < 10^{-9}$ indicates the termination of the iteration, and accordingly, the estimates of AOED are the output; otherwise, proceed to Step 6.

Step 6. Let $k \leftarrow k + 1$ *and return to Step 2*

Experimental data and evaluation metrics. We used numerical phantoms to demonstrate the validity and evaluate the performance of the proposed method considering the lack of enough ground truth for human tubular structures. As shown in Figure 2, we generated the simple phantoms containing dot-grid and the complex phantoms mimicking coronary arterial vessels with plaque burdens. In the simple phantom, there are 25 dots with the radius of 0.03 mm evenly distributed along the angle of 0°, 45°, 90°, 135°, 180°, 225°, and 270° in the imaging plane. The complex vessel phantoms contain multilayered tissues with different compositions varying from healthy tissues to rupture-prone plaques. The size of the imaging plane is 3 mm × 3 mm. By referring to histological findings on human arterial vessels,[55,56] we selected the optical and acoustic properties and geometrical parameters of different types of tissues, as shown in Table 2. The speed of sound and mass density of the vessel phantoms follow the Gaussian distributions based on the values provided in the table. We achieved the optical fluence simulation by discretely solving the DE with the finite difference time-domain algorithm. The forward acoustic process, including initial pressure signal generation and acoustic propagation, was simulated using the *k*-wave toolbox.[57] The sampling voltage signal output by the detector in response to the acoustic pressure reaching its receiving surface was generated based on equation (3). The noise vector was selected as an uncorrelated Gaussian white noise with zero mean and an SNR of 10 dB. The SD σ was determined by $\sigma = 0.03 \max[\hat{\boldsymbol{u}}_e]$, where $\max[\hat{\boldsymbol{u}}_e]$ is the maximal component of the theoretical sampling voltage vector without noise.[12] The SIR vector from the detector position to each location in the imaging domain was generated using the Field II simulation toolbox of MATLAB,[58] and the EIR was obtained by referring to Sheng *et al.*[32] as shown in Figure 3.

Table 2. Characteristic parameters of simple dot-grid phantom and coronary vessel phantoms.

Tissue name	Tissue composition	Refractive index	μ_a (cm^{-1})	μ_s (cm^{-1})	Anisotropy factor	Speed of sound (m/s)	Mass density (kg/L)	Radial thickness (mm)
Dot target	–	1.40	0.99	450	0.80	1635	1.30	0.03
Vessel wall adventitia	Connective tissue	1.39	0.70	5	0.80	1600	1.02	0~0.5
Vessel wall media	Muscular tissue	1.39	0.40	5	0.80	1580	1.07	0.1~0.4
Vessel wall intima	Muscular tissue	1.39	0.20	5	0.80	1560	1.07	0.2~0.5
Calcified plaque	Calcium	1.42	0.60	550	0.80	1650	0.94	0.01~0.25
Lipid-rich plaque	Lipid	1.42	0.90	500	0.80	1500	0.96	0.1~0.3
Macrophage	White blood cell	1.42	0.96	450	0.80	1620	0.97	0.1~0.2
Necrotic core	Nucleus	1.42	0.80	450	0.80	1620	0.97	0.1~0.2
Mixed calcified plaque	Calcium	1.42	0.60	550	0.80	1650	0.94	0.01~0.3
Vascular lumen	Blood	1.32	1.00	600	0.99	1540	1.13	1.2~1.7

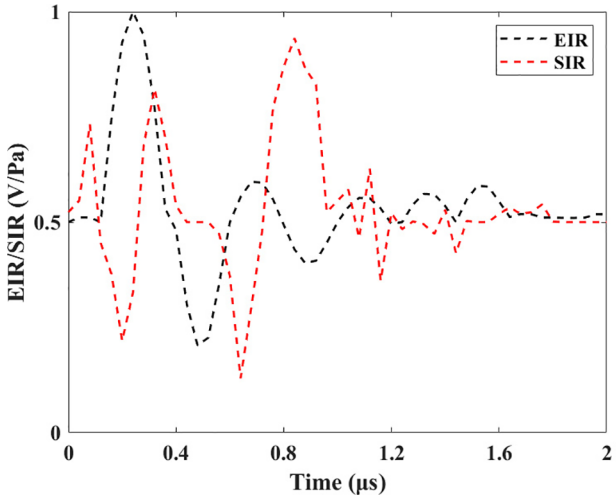

Figure 3. Profiles of EIR and SIR of the detector concerning time. (A color version of this figure is available in the online journal.)

In addition to visual inspection, we also quantitatively evaluated the quality of reconstructed images using standard metrics, including peak signal-to-noise ratio (PSNR), structural similarity index measure (SSIM), and normalized mean square absolute distance (NMSAD).[59] PSNR evaluates the image quality based on error sensitivity. NMSAD and SSIM measure the similarity between the reconstructed and ground truth images. High PSNR, high SSIM, or low NMSAD suggests reconstructions with high quality. In this work, the result images obtained by simulation were regarded as the ground truth images.

The conventional BP[53] and Wang's iterative reconstruction method[12] were employed to make a comparison with the method proposed in this work. Wang's method was developed for reconstructing three-dimensional PAT images based on an imaging model incorporating detector properties. As it utilized the conjugate gradient (CG) algorithm as the optimization framework, we call the CG method below for brevity. The programming environment of our experiments is MATLAB (R2018a, The MathWorks, Inc., Natick, MA, USA) on a personal computer configured with a 2.11 GHz Intel® Core™ i5-10210U CPU, 8 GB RAM, and Windows 10 64 bits as the operating system.

Results

Results of image reconstruction

Figures 4(a) and 5(a) show the ground truth images of the simple phantom and vessel phantoms obtained by numerical simulation. The images represent the maps of the spatially varying AOED. Figures 4(b) to (d) and 5(b) to (d) highlight the images reconstructed with the conventional BP, CG method, and our method, respectively. In the traditional BP reconstructions, a point-like ultrasonic transducer was assumed. In our approach, the initial AOED in the iteration was set to 0.9. From the figures, we can find that our approach improved the spatial resolution of the images as compared to the BP reconstructions. The images reconstructed by iterative inversion of the forward imaging model incorporating the detector responses can display the inner structures of different tissue types such as atherosclerotic plaques with various components embedded into the vessel wall. In contrast, these structures are significantly blurred in the images recovered by the traditional BP. Moreover, our approach outperforms the CG method in recovering the AOED distribution. The images obtained by our method are more similar to the forward simulations, represented by the PSNR, SSIM, and NMSAD results in Figure 6. The convergence of CG minimization highly depends upon both appropriate values of the initial guess and the termination conditions of the iteration. An unreasonable initial guess will lead to an unsatisfactory convergence. The termination condition directly determines the iteration times. Too many or too few iterations will lead to low accuracy of the solution, thereby affecting the quality of the reconstructed images. Therefore, it is essential to select the appropriate iteration termination conditions.

Influence of the optimization framework

The model-based reconstruction scheme must use appropriate optimization algorithms and regularization tools to solve the NLS problem effectively. We designed three experiments to discuss the influence of various optimization algorithms combined with different regularization tools on the reconstructions by our method.

First, we compared the reconstructions using FISTA combined with L1, total variation (TV), and the Tikhonov

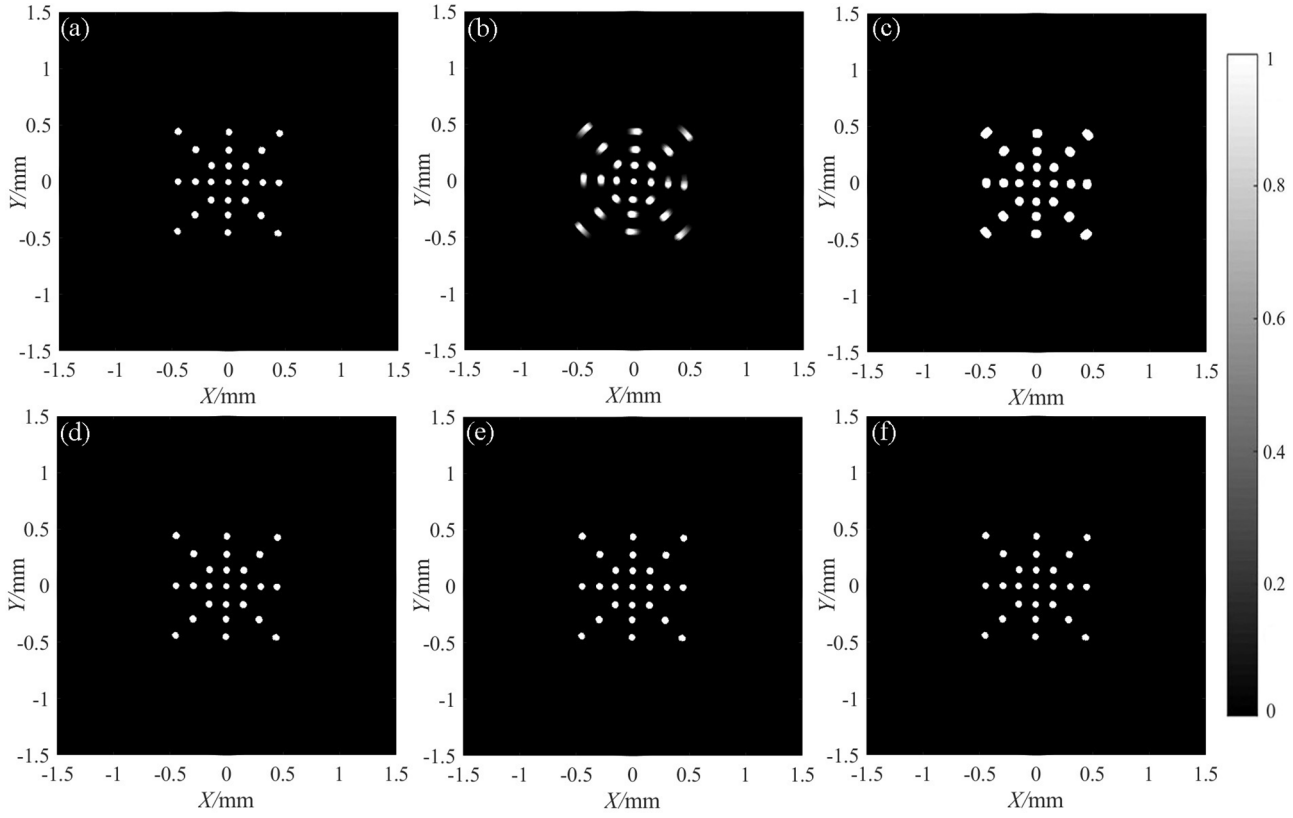

Figure 4. Image results of the simple phantom. (a) Ground truth image, (b) BP reconstruction, (c) CG reconstruction, (d) reconstruction with our method (FISTA + L1), (e) reconstruction with FISTA + TV, and (f) reconstruction with FISTA + Tikhonov.

regularization. Figures 4(d) to (f) and 7 show the results that exhibit no significant difference between the visualization of the reconstructed images. The evaluation metrics provided in Figure 8 indicate better quality of the reconstructions by FISTA + L1 than FISTA + TV and FISTA + Tikhonov.

Second, we compared the performances of four optimization algorithms, Broyden–Fletcher–Goldfarb–Shanno (BFGS) quasi-Newton, CG,[12] Levenberg–Marquardt (L-M),[60] and FISTA, each combined with L1 regularization in solving the NLS problem depicting the model-based image reconstruction. The results in Figures 9 to 11 indicate that FISTA + L1 and BFGS + L1 outperform CG + L1 and L-M + L1.

The L-M algorithm combines the steepest descent with the Gauss–Newton method to find the optimal value quickly. By updating the damping parameter, its parameter update is varied between the steepest descent update and the Gauss–Newton update. A small damping parameter leads to an update of Gauss–Newton, whereas a large one corresponds to the steepest descent update.[54] The steepest descent might converge to different local minima because the descent is fast when the estimated parameters are far from their optimums at the beginning of the iteration. In contrast, it is slow when the parameters are close to their optimums. The Gauss–Newton method might also converge to local minima if the initial guess is far from the optimal solution due to a too sizable iterative step size. In addition, the reconstruction quality of FISTA + L1 is slightly better than that of BFGS + L1 since the BFGS convergence value depends on the eigenvalues of the Hessian matrix. The larger the eigenvalues, the more iterations are required to correct them. As shown in Figure 11, FISTA requires the least iteration times to converge to the global minimum among the four algorithms.

Third, we conducted experiments to analyze the influence of various regularization tools on the reconstruction quality by BFGS. From the results shown in Figures 12 and 13, we found that BFGS + L1 can achieve better reconstruction quality than BFGS + TV and BFGS + Tikhonov, demonstrating that changing the regularization term does not improve the quality of reconstructions by BFGS.

Influence of the initial guess of iterations

We changed the initial AOED in iteration while letting the other parameters remain unchanged to discuss the dependence of our method on the values of the initial guess. Figures 14 and 15 provide the results in the cases of $A_0(\boldsymbol{r}) = 0.3$, 0.6, and 0.9, respectively, which demonstrate the robustness of our method concerning the initial guess of iteration.

Discussion

Image reconstruction is an essential issue in PAT imaging. The method used to reconstruct tomographic images depends on the complexity of the imaged structures, collecting the photoacoustically induced acoustic waves, and the type of detector. EPAT is an endoscopic application of PAT to visualize the anatomical structures and functional compositions of biological tubular structures. Its scanning aperture is

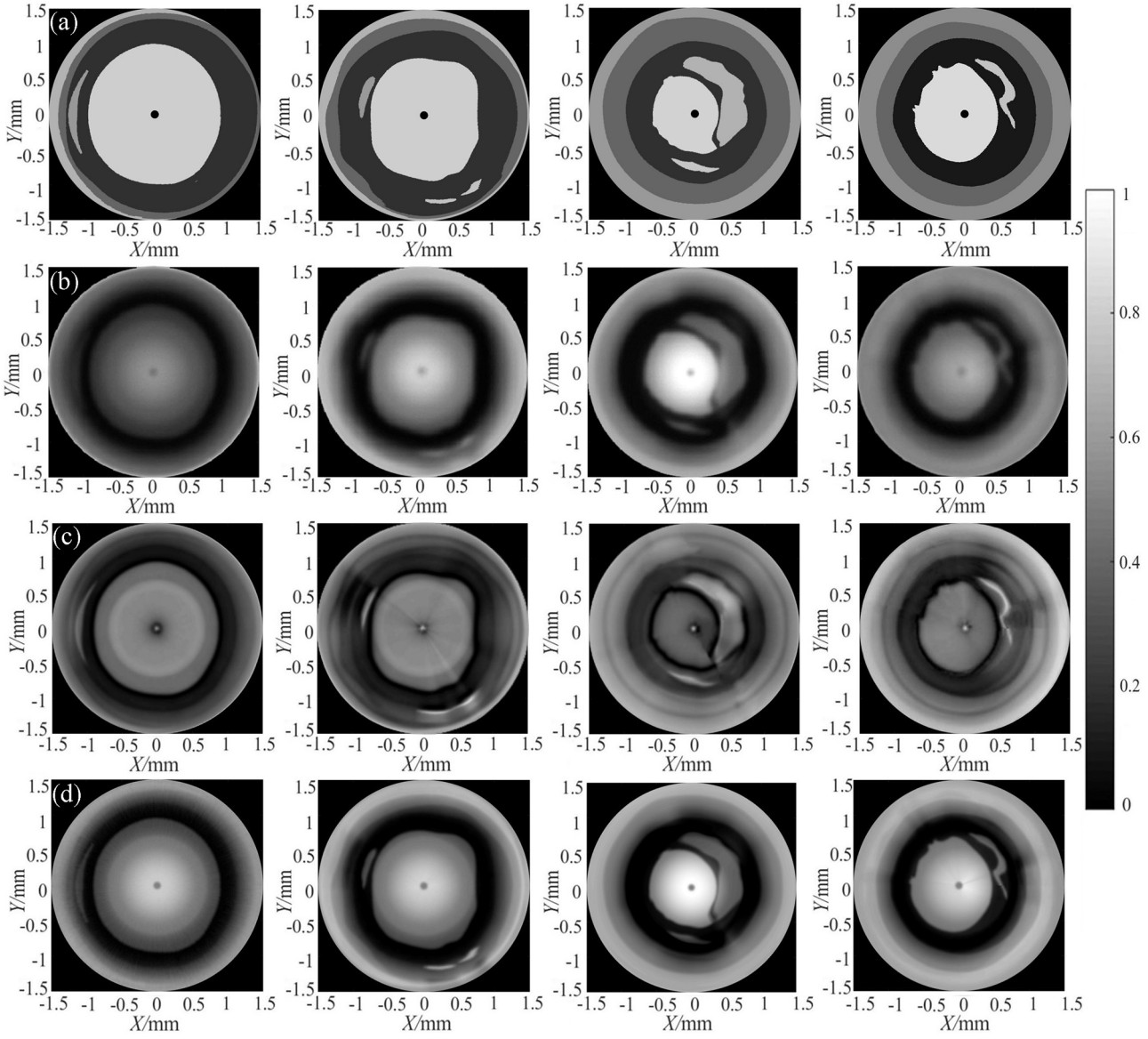

Figure 5. Image results of the vessel phantoms. (a) Ground truth images and (b) to (d) images reconstructed with BP, CG, and our method, respectively.

enclosed in a digest cavity or a vascular lumen with complex geometry. Therefore, sparsely sampling in a limited view is inevitable owing to the limitation of the mechanical structures of the catheter. EPAT cannot directly use well-developed PAT image reconstruction methods. On the contrary, the reconstruction methods developed especially for EPAT cannot be applied to PAT without any changes. This study focuses on reconstruction enhancement techniques for EPAT rather than general PAT.

The model-based image reconstruction is essentially the inversion of a forward operator, such that the reconstruction accuracy relies strongly on accurate forward modeling. The forward model of photoacoustic imaging includes optical model, acoustic model, and ultrasonic detection model. The optical model describes the transmission of incident light in the tissue, and the acoustic model depicts the propagation of photoacoustic waves in the tissue. The two are coupled by the thermoelastic effect. RTE is a widely accepted physical model of light transmission in turbid media. Given the light source, the geometry of the imaging target, and optical parameters of the imaging medium, solving the RTE produces the theoretical light fluence. However, the solution of the RTE is a computationally burdensome task since it is an integrodifferential equation in phase space. Discretization is required in both space domain and angle domain. Therefore, its approximations are generally applied in optical imaging, such as the diffusion approximation and Monte Carlo (MC).[61] The diffusion approximation is a deterministic model based on which the RTE is simplified as the DE. The solution of the DE is relatively simple in that discretization is needed only in the space domain. However, the diffusion approximation is only valid in the diffusion domain, that is, the region of several mean free paths from the light source. For PAT, the area close to the light source and the imaging domain boundary constitute essential parts of the recovered image. They usually contain crucial information required for the evaluation

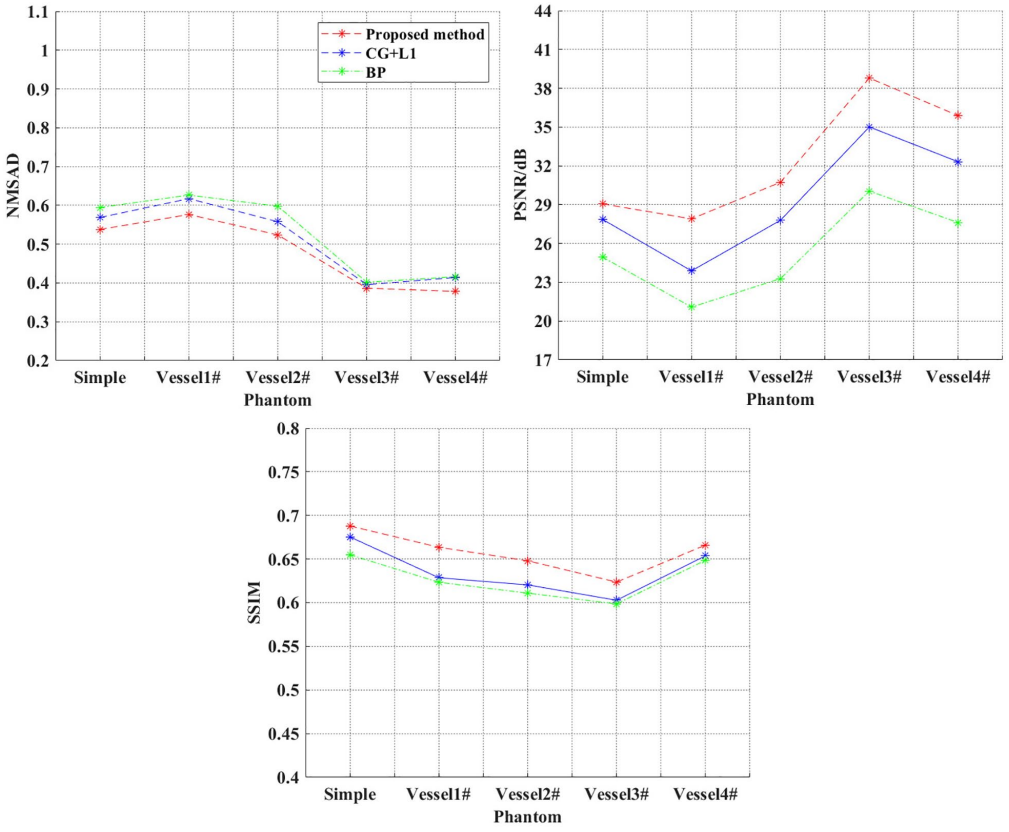

Figure 6. Evaluation metrics of the images reconstructed with BP, CG, and our method, respectively. (A color version of this figure is available in the online journal.)

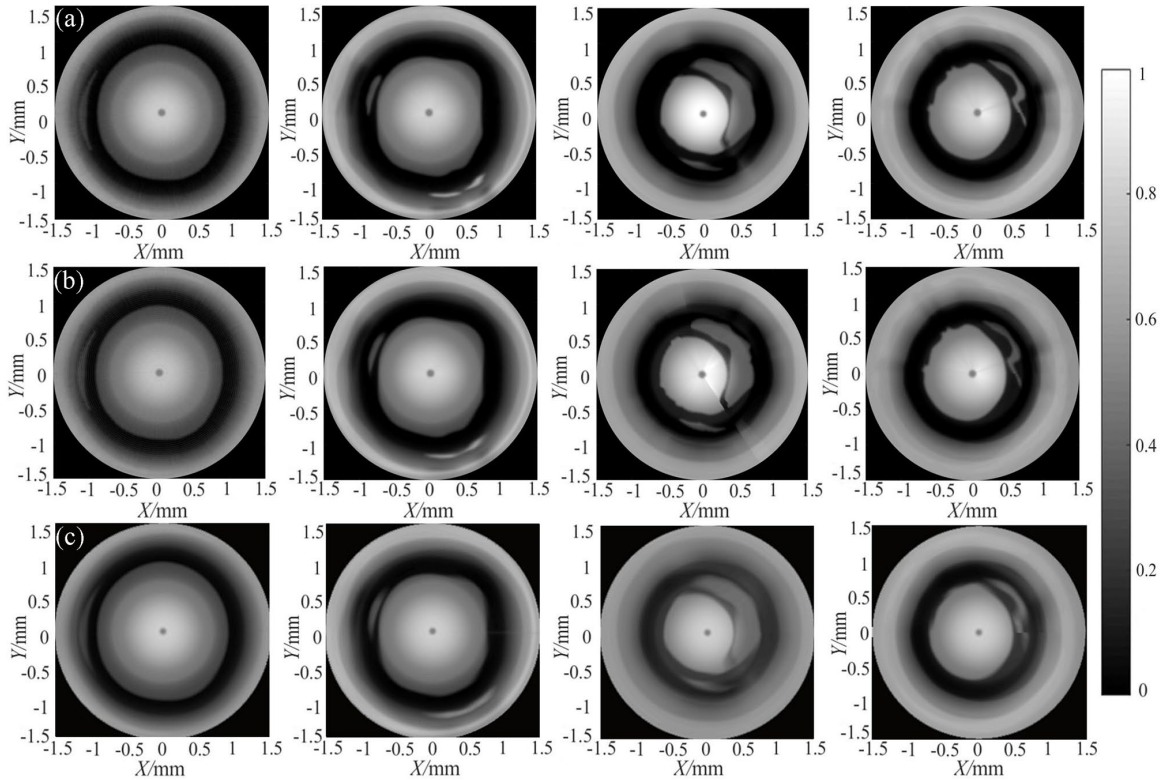

Figure 7. Images of the vessel phantoms reconstructed with FISTA optimization. (a) FISTA + L1, (b) FISTA + TV, and (c) FISTA + Tikhonov.

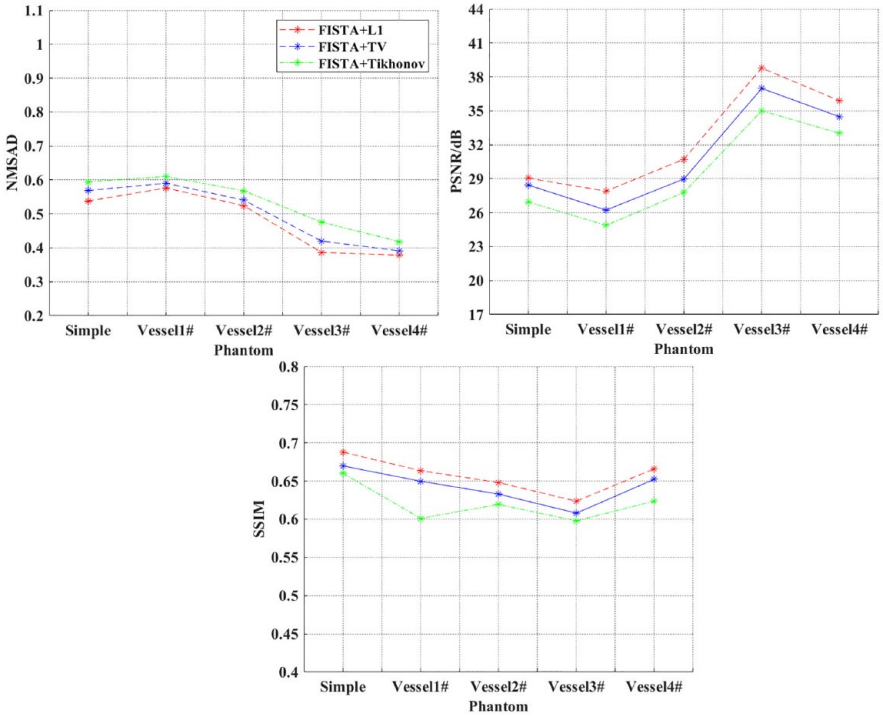

Figure 8. Evaluation metrics of the images shown in Figures 4(d) to (f) and 7. (A color version of this figure is available in the online journal.)

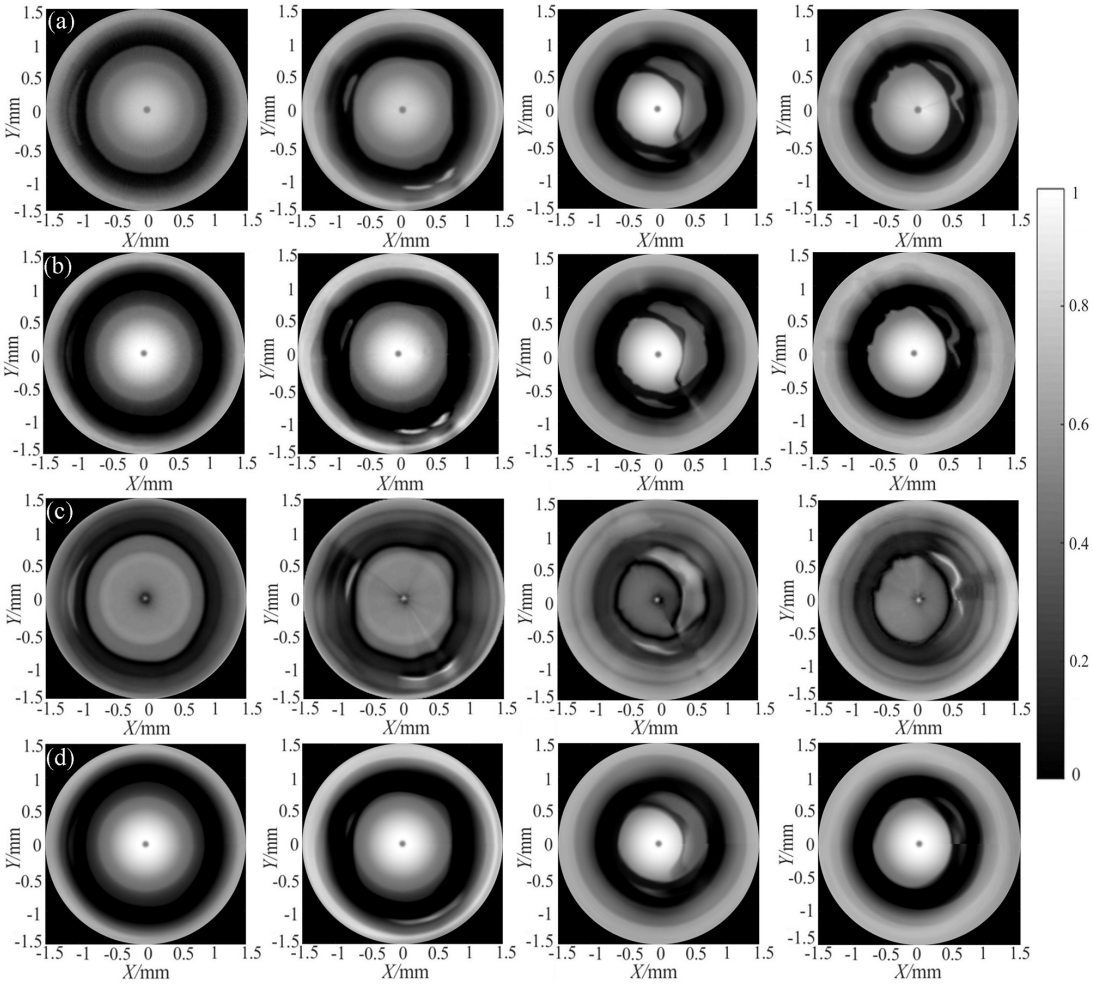

Figure 9. Images of the vessel phantoms reconstructed with different optimization schemes. (a) FISTA + L1, (b) BFGS + L1, (c) CG + L1, and (d) LM + L1.

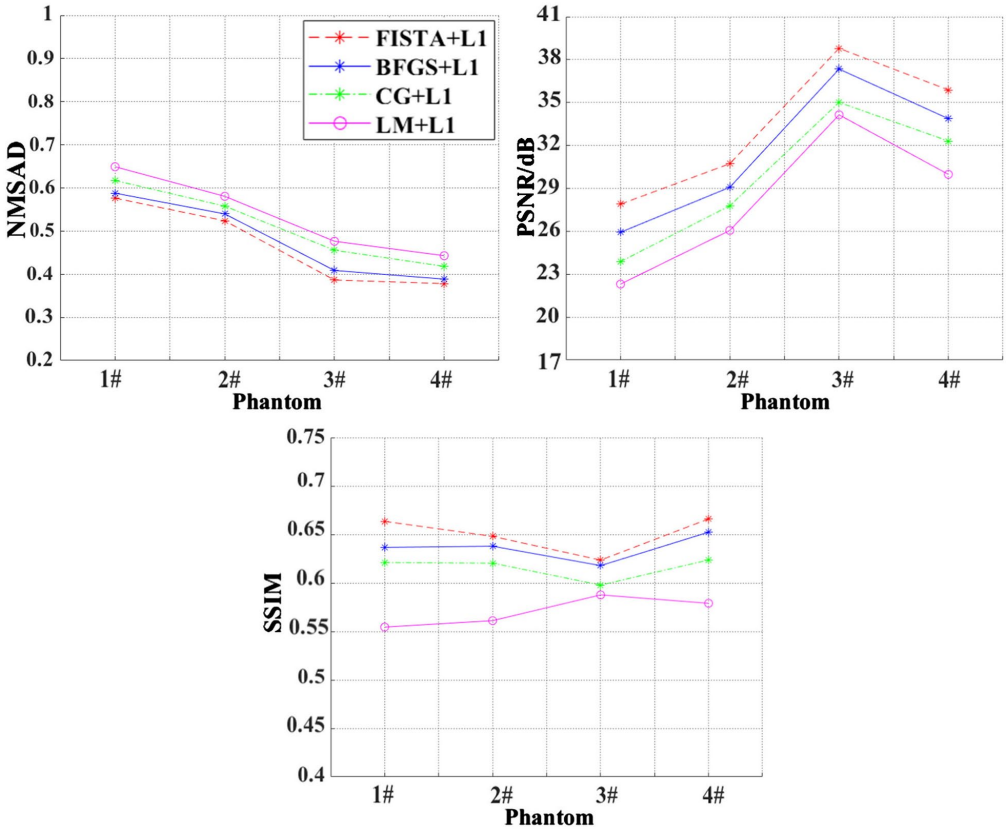

Figure 10. Evaluation metrics of the images shown in Figure 9. (A color version of this figure is available in the online journal.)

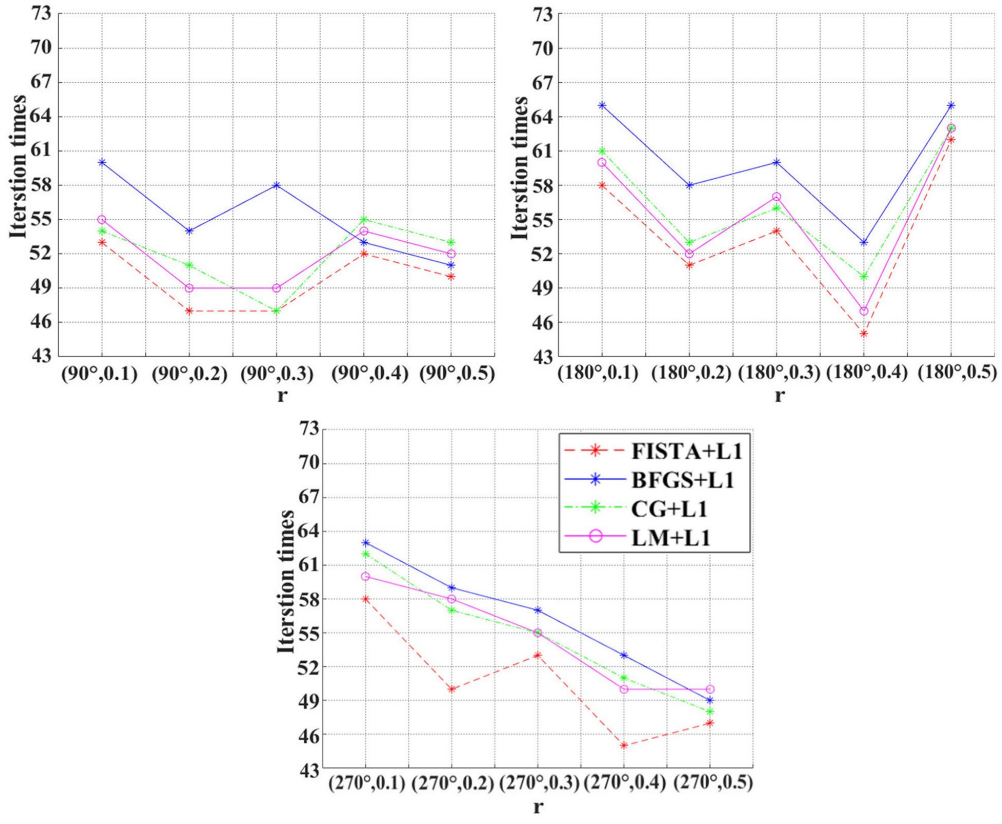

Figure 11. Iteration times for recovering the AOED at several locations in the cross-section of vessel phantom I with different optimization algorithms. (A color version of this figure is available in the online journal.)

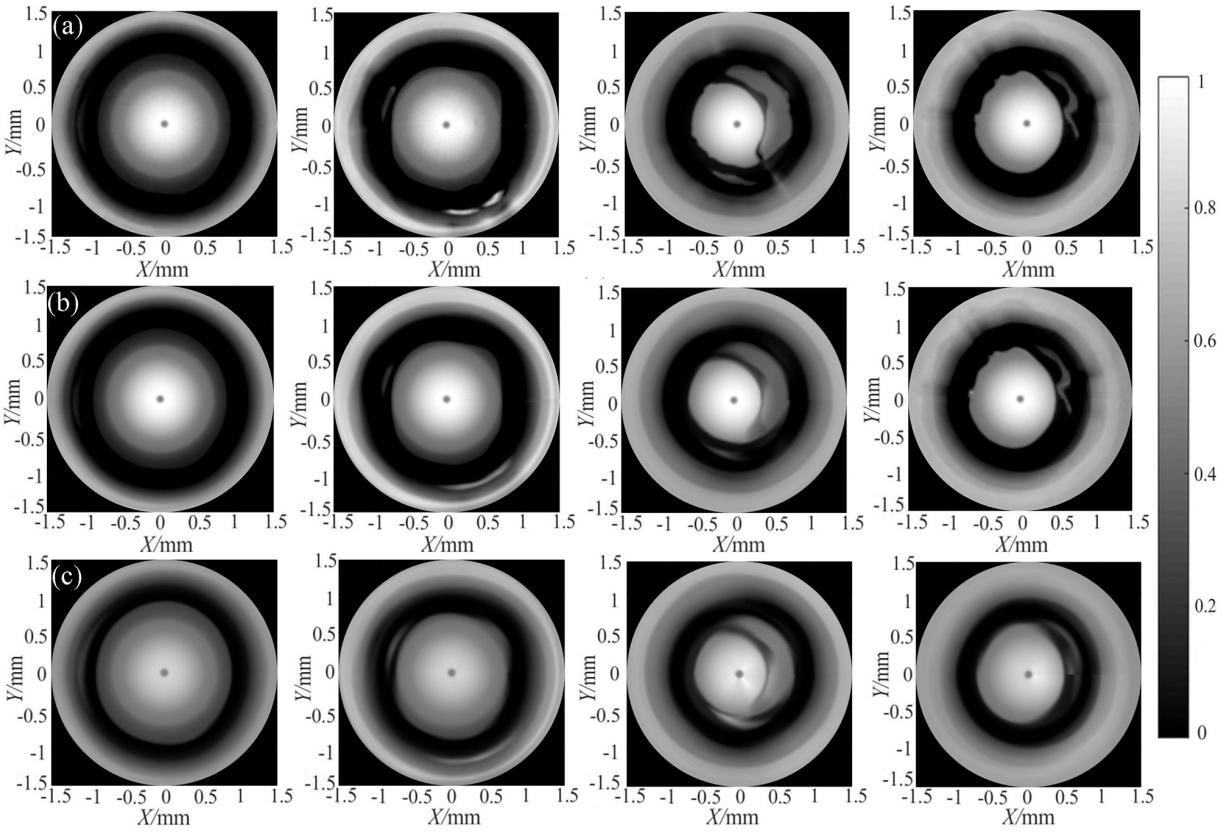

Figure 12. Images of the vessel phantoms reconstructed with BFGS optimization. (a) BFGS + L1, (b) BFGS + TV, and (c) BFGS + Tikhonov.

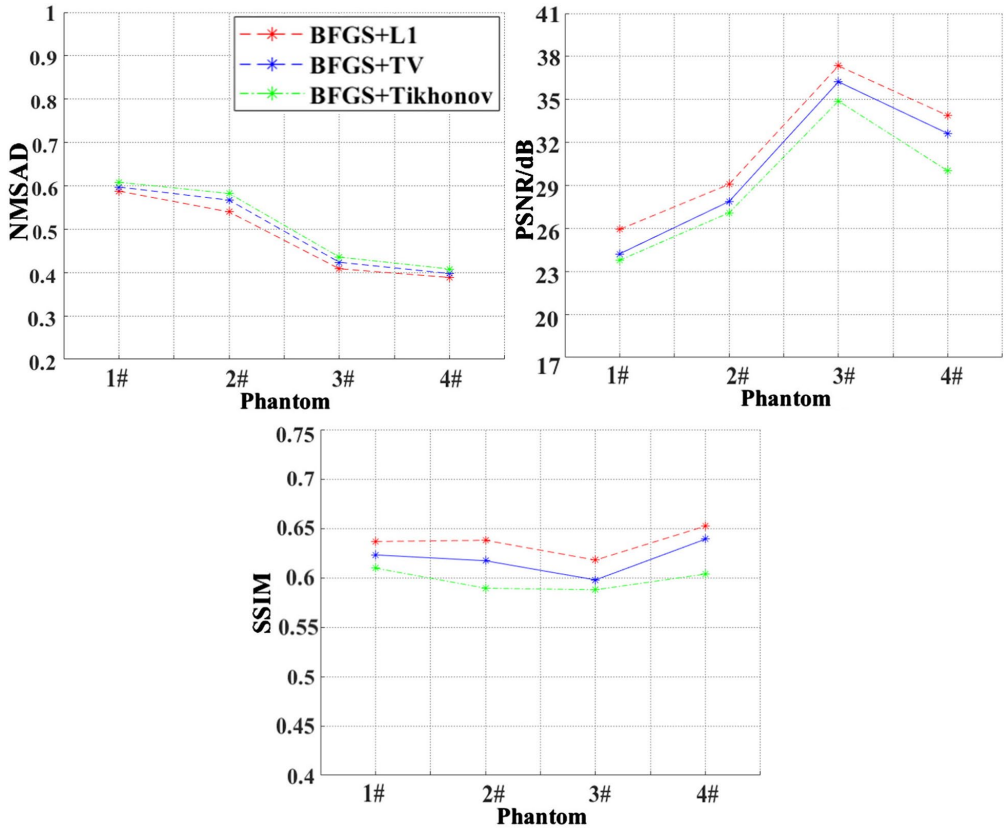

Figure 13. Evaluation metrics of the images shown in Figure 12. (A color version of this figure is available in the online journal.)

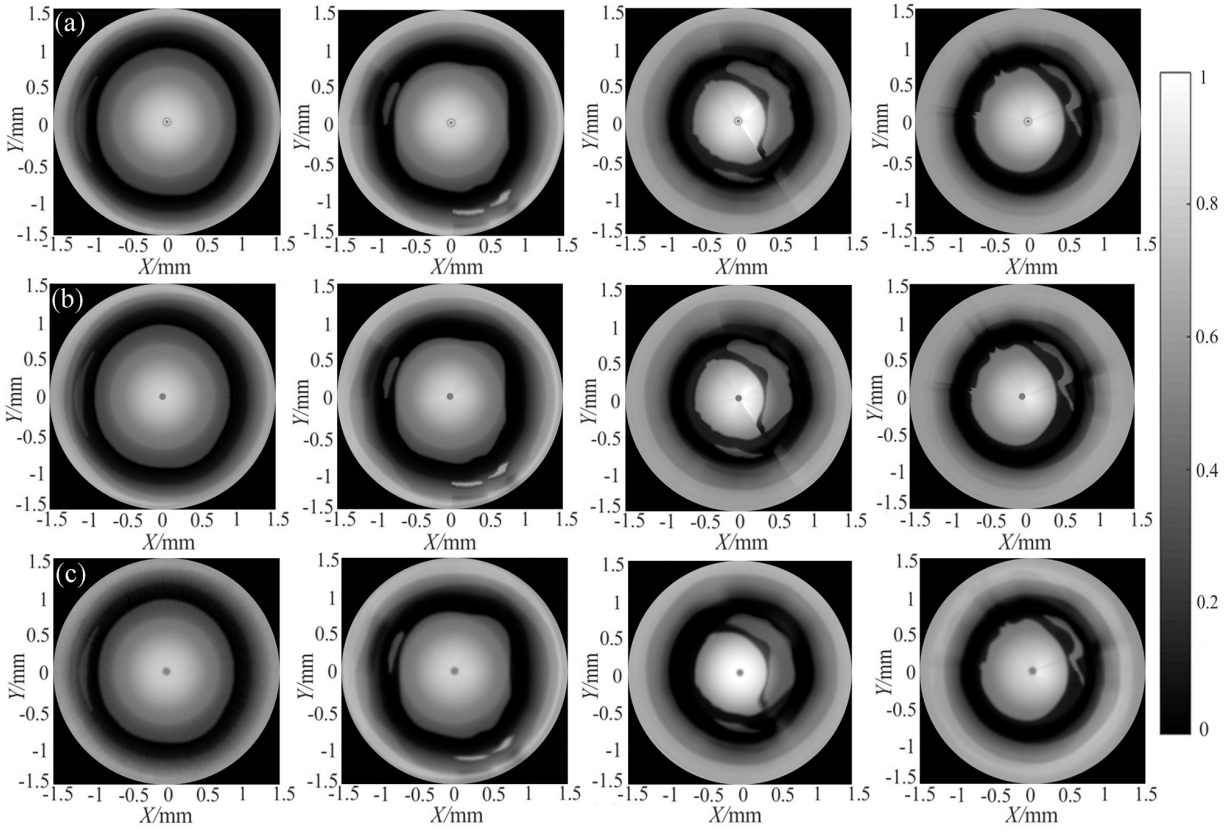

Figure 14. Images of the vessel phantoms reconstructed with different initial values of AOED. (a) 0.3, (b) 0.6, and (c) 0.9.

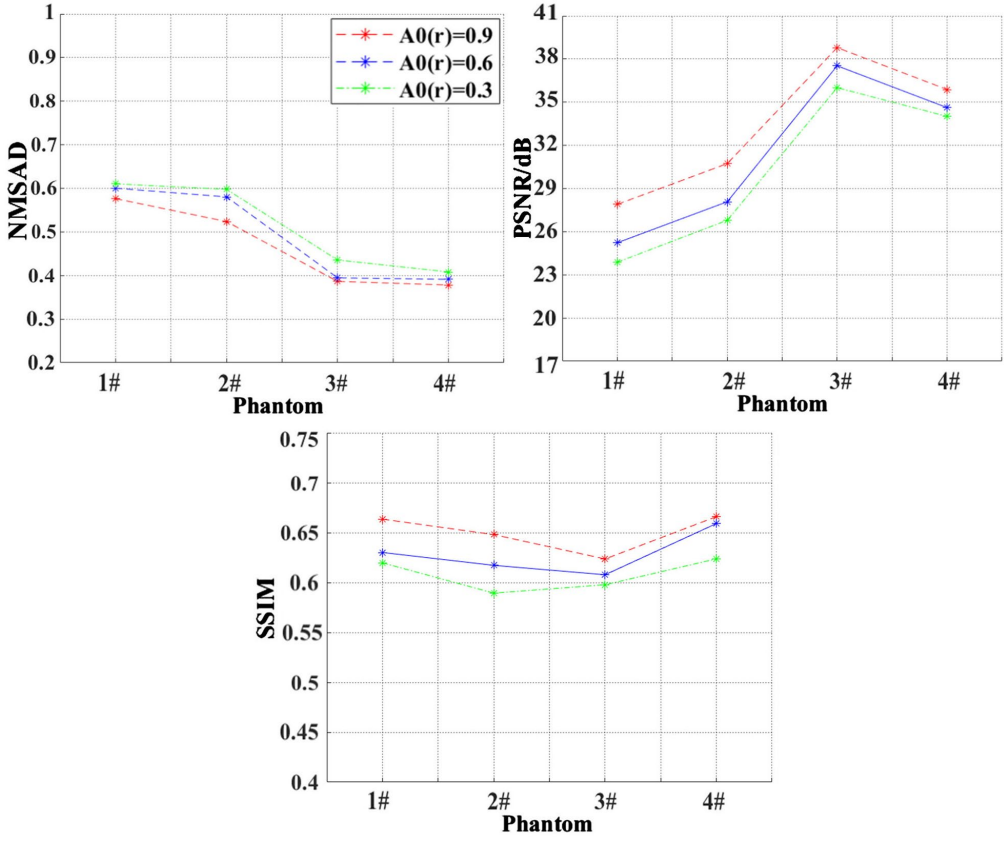

Figure 15. Evaluation metrics of the images shown in Figure 14. (A color version of this figure is available in the online journal.)

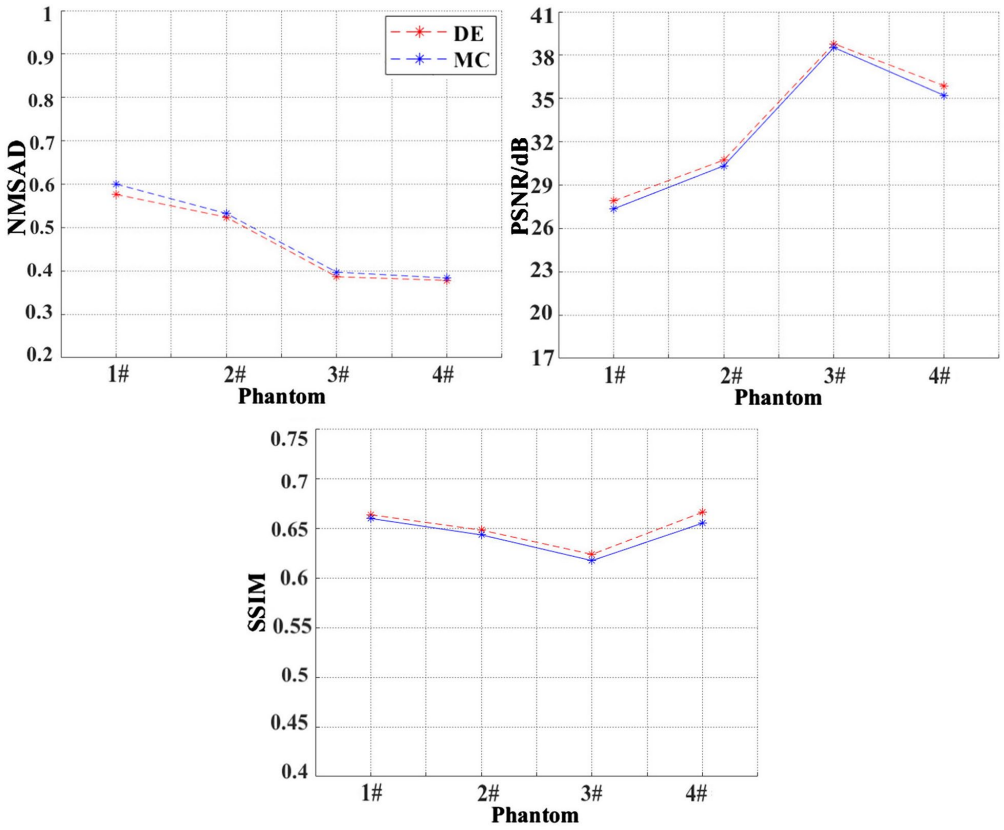

Figure 16. Evaluation metrics of reconstructed images when using DE and MC for light transport modeling, respectively. (A color version of this figure is available in the online journal.)

of diseased tissues. Light transmission in these regions is highly anisotropic, so the diffusion approximation does not hold. Alternatively, MC is a stochastic method that simulates interactions between light and tissues. A calculative brief model of light propagation in turbid media is required in the model-based image reconstruction algorithms because the forward operator is calculated repeatedly during iteration. Therefore, this would consider the computational and accuracy trade-offs between DE and MC to better determine what situations would be used. Figures 16 and 17 provide the image results of DE and MC, respectively. The results reveal insignificant differences between the quality of the final reconstructions by DE and MC, while MC is computationally burdensome than DE. These results suggest that the possible inaccuracy of DE in modeling light transport in the regions where the diffusion approximation is invalid is tolerable in terms of the significant improvement in the image quality and computational cost.

In addition, the image reconstruction algorithm should take the detector properties into account to improve the image quality. In this work, we only incorporated the spatial and temporal responses of the detector into the forward model. However, in practical applications, the detector directionality,[62] limited aperture,[11] limited view,[63] limited bandwidth,[64] scanning radius,[65] and the uncertainty of detector position[66] affect the reconstruction quality apart from the EIR and SIR. We will optimize the accuracy of the forward model further in our future work by incorporating these detector properties into the model, ultimately improving the quality of reconstructed images.

In addition, even though promising results have been obtained with simulation data, verifying the fidelity of the recovered structures for *in vivo* images is still technically challenging. It is a common problem in image reconstruction and enhancement methods due to the lack of ground truth information on the underlying tissue properties when acquiring experimental measurements.[64] Our future work will validate our approach on *in vivo* data.

Conclusions

We designed a method for EPAT image reconstruction considering the detector responses. We incorporated the SIR and EIR of the detector into the forward model. We then reconstructed the cross-sectional images representing the AOED distribution based on the sampling voltage signals by iteratively solving the inverse problem of the forward model. The results of the simulation data demonstrated the improvement of the reconstruction quality by our method compared with conventional BP and the previous CG method. Our comparison results indicate that the image quality reconstructed with FISTA + L1-regularization is better than FISTA + TV-regularization and FISTA + Tikhonov-regularization. In contrast, FISTA is superior to BFGS, CG, and L-M when L1 regularization is used. In addition, our model-based reconstruction based on FISTA + L1

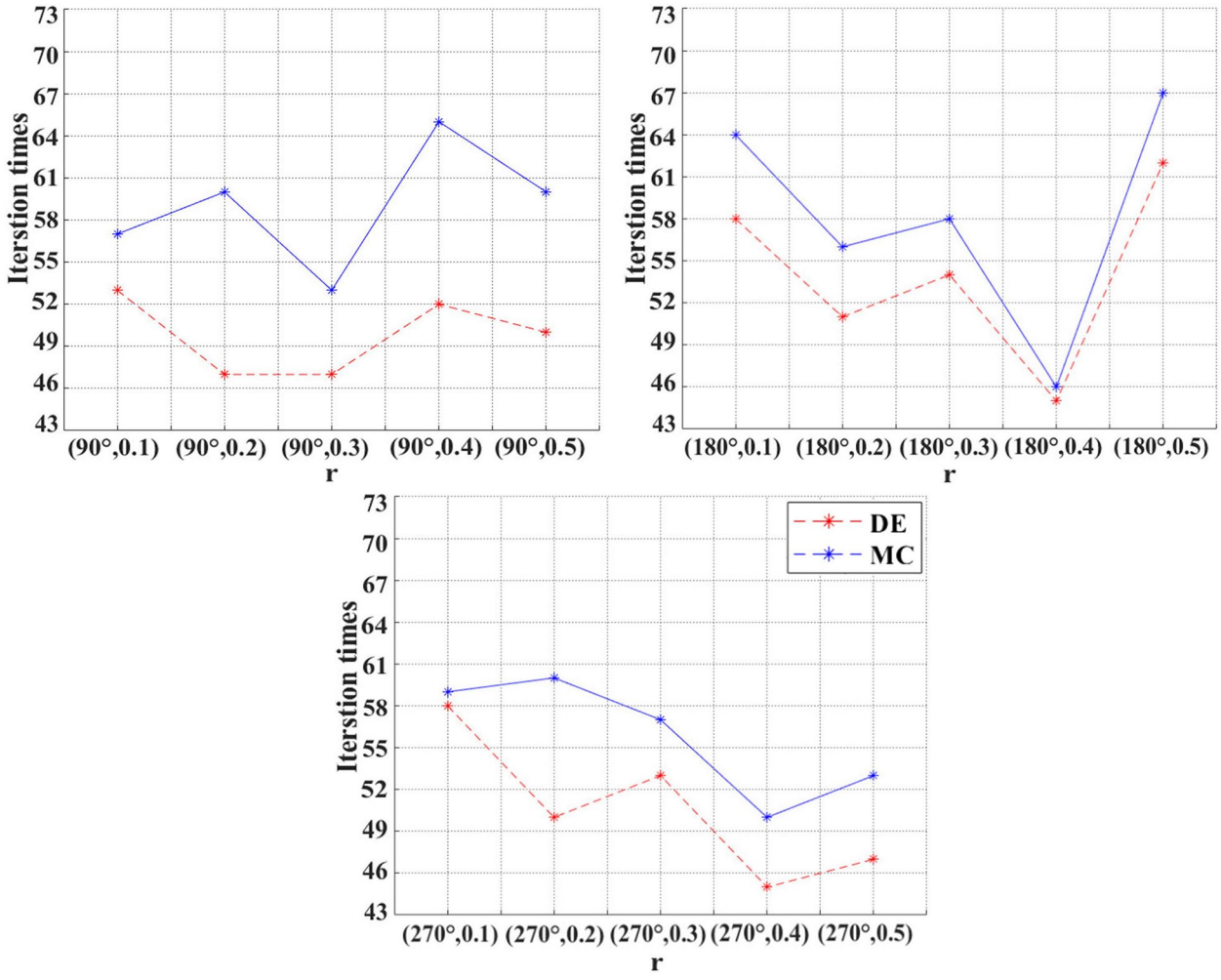

Figure 17. Iteration times for recovering the AOED at several locations in the cross-section of vessel phantom I when DE and MC are used for light transport modeling, respectively. (A color version of this figure is available in the online journal.)

optimization has been demonstrated to be robust to the initial guess of iteration.

AUTHORS' CONTRIBUTIONS

All the authors contributed to the experimental and model design, data analysis, and manuscript writing.

DECLARATION OF CONFLICTING INTERESTS

The author(s) declared no potential conflicts of interest with respect to the research, authorship, and/or publication of this article.

FUNDING

The author(s) disclosed receipt of the following financial support for the research, authorship, and/or publication of this article: This work was supported by the National Nature Science Foundation of China (no. 62071181).

ORCID ID

Zheng Sun https://orcid.org/0000-0002-7066-2320

REFERENCES

1. Xu M, Wang LV. Universal back-projection algorithm for photoacoustic computed tomography. *Phys Rev E Stat Nonlin Soft Matter Phys* 2005; **71**:016706
2. Kong Q, Gong R, Liu J, Shao X. Investigation on reconstruction for frequency domain photoacoustic imaging via TVAL3 regularization algorithm. *IEEE Photonics J* 2018;**10**:3901215
3. Shang R, Archibald R, Gelb A, Luke GP. Sparsity-based photoacoustic image reconstruction with a linear array transducer and direct measurement of the forward model. *J Biomed Opt* 2019;**24**:031015
4. Wang B, Su T, Pang W, Wei N, Xiao J, Peng K. Back-projection algorithm in generalized form for circular-scanning-based photoacoustic tomography with improved tangential resolution. *Quant Imaging Med Surg* 2019;**9**:491–502
5. Spadin F, Jaeger M, Nuster R, Subochev P, Frenz M. Quantitative comparison of frequency-domain and delay-and-sum optoacoustic image reconstruction including the effect of coherence factor weighting. *Photoacoustics* 2020;**17**:100149
6. Sun Z, Han D, Yuan Y. 2-D image reconstruction of photoacoustic endoscopic imaging based on time-reversal. *Comput Biol Med* 2016;**76**:60–8
7. Javaherian A, Holman S. A multi-grid iterative method for photoacoustic tomography. *IEEE Trans Med Imaging* 2017;**36**:696–706
8. Bai MR, Chung C, Lan SS. Iterative algorithm for solving acoustic source characterization problems under block sparsity constraints. *J Acoust Soc Am* 2018;**143**:3747–57
9. Poudel J, Yang L, Anastasio MA. A survey of computational frameworks for solving the acoustic inverse problem in three-dimensional photoacoustic computed tomography. *Phys Med Biol* 2019;**64**:14TR01
10. Xu M, Wang LV. Analytic explanation of spatial resolution related to bandwidth and detector aperture size in thermoacoustic or photoacoustic reconstruction. *Phys Rev E* 2003;**67**:1–15

11. Tian C, Pei M, Shen K, Liu S, Hu Z, Feng T. Impact of system factors on the performance of photoacoustic tomography scanners. *Phys Rev Appl* 2020;**13**:014001
12. Wang K, Ermilov SA, Su R, Brecht HP, Oraevsky AA, Anastasio MA. An imaging model incorporating ultrasonic transducer properties for three-dimensional optoacoustic tomography. *IEEE Trans Med Imaging* 2011;**30**:203–14
13. Li ML, Zhang HE, Maslov K, Stoica G, Wang LV. Improved in vivo photoacoustic microscopy based on a virtual-detector concept. *Opt Lett* 2006;**31**:474–6
14. Li ML, Wang LV. A study of reconstruction in photoacoustic tomography with a focused transducer. In: *SPIE international conference on photons plus ultrasound: imaging and sensing 2007: the eighth conference on biomedical thermoacoustics, optoacoustics, and acousto-optics 64371E (SPIE, 2007)*, vol. 6437, San Jose, CA, 20–25 January 2007
15. Li CH, Wang LV. High-numerical-aperture-based virtual point detectors for photoacoustic tomography. *Appl Phys Lett* 2008;**93**:033902
16. Li C, Ku G, Wang LV. Improving the image quality of photoacoustic tomography (PAT) by using a negative acoustic lens. In: *SPIE international conference on photons plus ultrasound: imaging and sensing 2008: the ninth conference on biomedical thermoacoustics, optoacoustics, and acousto-optics 685623 (SPIE, 2008)*, vol. 6856, San Jose, CA, 19–24 January 2008
17. Pramanik M, Ku G, Wang LV. Tangential resolution improvement in thermoacoustic and photoacoustic tomography using a negative acoustic lens. *J Biomed Opt* 2009;**14**:024028
18. Han J, Gui Z, Wen T, Tian E, Yang P, Zhang Q. Direct and real-time subwavelength resolution photoacoustic imaging method based on acoustic lens with negative refractive index. *J Meas Sci Instrum* 2016;**7**:388–97
19. Chiu CH, Chuo Y, Li M. Image reconstruction of photoacoustic tomography based on finite-aperture-effect corrected compressed sensing algorithm. In: *SPIE international conference on photons plus ultrasound: imaging & sensing 89433X (SPIE, 2014)*, vol. 8943, San Francisco, CA, 1–6 February 2014
20. Rosenthal A, Ntziachristos V, Razansky D. Model-based optoacoustic inversion with arbitrary-shape detectors. *Med Phys* 2011;**38**:4285–95
21. Dean-Ben XL, Buehler A, Ntziachristos V, Razansky D. Accurate model-based reconstruction algorithm for three-dimensional optoacoustic tomography. *IEEE Trans Med Imaging* 2012;**31**:1922–8
22. Araque Caballero MA, Gateau J, Dean-Ben XL, Ntziachristos V. Model-based optoacoustic image reconstruction of large three-dimensional tomographic datasets acquired with an array of directional detectors. *IEEE Trans Med Imaging* 2014;**33**:433–43
23. Liu F, Gong X, Wang LV, Guan J, Meng J. Dictionary learning sparse-sampling reconstruction method for in-vivo 3D photoacoustic computed tomography. *Biomed Opt Express* 2019;**10**:1660–77
24. Lu D, Déan-Ben XL, Razansky D. 20 frames per second model-based reconstruction in cross-sectional optoacoustic tomography. In: *SPIE international conference on photons plus ultrasound: imaging and sensing 100641A*, vol. 10064, San Francisco, CA, 28 January–2 February 2017
25. Ding L, Dean-Ben XL, Razansky D. Efficient 3-D model-based reconstruction scheme for arbitrary optoacoustic acquisition geometries. *IEEE Trans Med Imaging* 2017;**36**:1858–67
26. Lu D, Razansky D, Déan-Ben XL. Model-based reconstruction of large three-dimensional optoacoustic datasets. *IEEE T Med Imaging* 2020;**39**:2931–40
27. Li ML, Cheng CC. Model-based reconstruction for photoacoustic tomography with finite aperture detectors. In: *IEEE international ultrasonics symposium*, Rome, 20–23 September 2009, pp. 2359–2362. New York: IEEE
28. Li ML, Tseng YC, Cheng CC. Model-based correction of finite aperture effect in photoacoustic tomography. *Opt Express* 2010;**18**:26285–92
29. Queirós D, Déan-Ben XL, Buehler A, Razansky D, Rosenthal A, Ntziachristo V, Ntziachristos V. Incorporating geometric detector properties into three-dimensional optoacoustic tomography. In: *SPIE international conference on opto-acoustic methods and applications 88000C (SPIE, 2013)*, vol. 8800, Munich, 12–16 May 2013
30. Mitsuhashi K, Wang K, Anastasio MA. Investigation of the far-field approximation for modeling a transducer's spatial impulse response in photoacoustic computed tomography. *Photoacoustics* 2014;**2**:21–32
31. Sheng Q, Wang K, Xia J, Zhu L, Wang LV, Anastasio MA. Photoacoustic computed tomography without accurate ultrasonic transducer responses. In: *SPIE international conference on photons plus ultrasound: imaging & sensing 932313 (SPIE, 2015)*, vol. 9323, San Francisco, CA, 7–12 February 2015
32. Sheng Q, Wang K, Matthews TP, Xia J, Zhu L, Wang LV, Anastasio MA. A constrained variable projection reconstruction method for photoacoustic computed tomography without accurate knowledge of transducer responses. *IEEE Trans Med Imaging* 2015;**34**:2443–58
33. Han Y, Ntziachristos V, Rosenthal A. A system analysis and image reconstruction tool for optoacoustic imaging with finite-aperture detectors. In: *SPIE international conference on opto-acoustic methods and applications in biophotonics II 953915 (SPIE, 2015)*, vol. 9539, Munich, 21–25 June 2015
34. Han Y, Ntziachristos V, Rosenthal A. Optoacoustic image reconstruction and system analysis for finite-aperture detectors under the wavelet-packet framework. *J Biomed Opt* 2016;**21**:16002
35. Drozdov G, Rosenthal A. Analysis of negatively focused ultrasound detectors in optoacoustic tomography. *IEEE Trans Med Imaging* 2017;**36**:301–9
36. Rabanser S, Neumann L, Haltmeier M. Stochastic proximal gradient algorithms for multi-source quantitative photoacoustic tomography. *Entropy* 2018;**20**:1–24
37. Drozdov G, Levi A, Rosenthal A. The impulse response of negatively focused spherical ultrasound detectors and its effect on tomographic optoacoustic reconstruction. *IEEE Trans Med Imaging* 2019;**38**:2326–37
38. Jin H, Zhang R, Liu S, Zheng Y. Fast and high-resolution three-dimensional hybrid-domain photoacoustic imaging incorporating analytical-focused transducer beam amplitude. *IEEE Trans Med Imaging* 2019;**38**:2926–36
39. Zhang C, Wang YY. Deconvolution reconstruction of full-view and limited-view photoacoustic tomography: a simulation study. *J Opt Soc Am A Opt Image Sci Vis* 2008;**25**:2436–43
40. Li M, Cheng C. Reconstruction of photoacoustic tomography with finite-aperture detectors: deconvolution of the spatial impulse response. In: *SPIE international conference on photons plus ultrasound: imaging & sensing 75642S (SPIE, 2010)*, vol. 7564, San Francisco, CA, 23–28 January 2010
41. Chen JH, Lin RQ, Wang HN, Meng J, Zheng HR, Song L. Blind-deconvolution optical-resolution photoacoustic microscopy in vivo. *Opt Express* 2013;**21**:7316–27
42. Prakash J, Raju AS, Shaw CB, Pramanik M, Yalavarthy PK. Basis pursuit deconvolution for improving model-based reconstructed images in photoacoustic tomography. *Biomed Opt Express* 2014;**5**:1363–77
43. Roitner H, Haltmeier M, Nuster R, O'Leary DP, Berer T, Paltauf G, Grun H, Burgholzer P. Deblurring algorithms accounting for the finite detector size in photoacoustic tomography. *J Biomed Opt* 2014;**19**:056011
44. Cai D, Li ZF, Li Y, Guo ZD, Chen SL. Photoacoustic microscopy in vivo using synthetic-aperture focusing technique combined with three-dimensional deconvolution. *Opt Express* 2017;**25**:1421–34
45. Moradi H, Tang S, Salcudean SE. Deconvolution based photoacoustic reconstruction with sparsity regularization. *Opt Express* 2017;**25**:2771–89
46. Luo X, Xiao J, Wang C, Wang B. Fast correction of "finite aperture effect" in photoacoustic tomography based on spatial impulse response. *Photonics* 2021;**8**:356
47. Rosenthal A, Ntziachristos V, Razansky D. Optoacoustic methods for frequency calibration of ultrasonic sensors. *IEEE Trans Ultrason Ferroelectr Freq Control* 2011;**58**:316–26
48. Wang B, Wei N, Peng K, Xiao J. Modified back-projection method in acoustic resolution-based photoacoustic endoscopy for improved lateral resolution. *Med Phys* 2018;**45**:4430–8
49. Choi SSS, Mandelis A. Review of the state of the art in cardiovascular endoscopy imaging of atherosclerosis using photoacoustic techniques with pulsed and continuous-wave optical excitations. *J Biomed Opt* 2019;**24**:1–15

50. Karlas A, Fasoula NA, Paul-Yuan K, Reber J, Kallmayer M, Bozhko D, Seeger M, Eckstein HH, Wildgruber M, Ntziachristos V. Cardiovascular optoacoustics: from mice to men-A review. *Photoacoustics* 2019; **14**:19–30
51. Zhao T, Desjardins AE, Ourselin S, Vercauteren T, Xia W. Minimally invasive photoacoustic imaging: current status and future perspectives. *Photoacoustics* 2019;**16**:100146
52. Li S, Montcel B, Yuan Z, Liu W, Vray D. Multigrid-based reconstruction algorithm for quantitative photoacoustic tomography. *Biomed Opt Express* 2015;**6**:2424–34
53. Xu M, Wang LV. Time-domain reconstruction for thermoacoustic tomography in a spherical geometry. *IEEE Trans Med Imaging* 2002; **21**:814–22
54. Bech A. A fast iterative shrinkage-thresholding algorithms for linear inverse problems. *SIAM J Imaging Sci* 2009;**2**:183–202
55. Jacques SL. Optical properties of biological tissues: a review. *Phys Med Biol* 2013;**58**:R37–61
56. Yamada M, Jinzaki M, Kuribayashi S, Sato K, Tanami Y, Yun S, Sasaki K. Evaluation of coronary artery lumen diameter with 16-slice multidetector-row computed tomography. *Circ J* 2005;**69**:1230–2
57. Treeby BE, Cox BT. k-Wave: MATLAB toolbox for the simulation and reconstruction of photoacoustic wave fields. *J Biomed Opt* 2010;**15**: 021314
58. Lu T, Wang Y, Li J, Prakash J, Gao F, Ntziachristos V. Full-frequency correction of spatial impulse response in back-projection scheme using space-variant filtering for optoacoustic mesoscopy. *Photoacoustics* 2020;**19**:100193
59. Herman GT. Image reconstruction from projection: The fundamentals of computerized tomography. New York: Academic Press, 1980
60. Moré JJ. The Levenberg-Marquardt algorithm: implementation and theory. In: Watson GA (ed.) *Numerical analysis*, vol. 630. Berlin; Heidelberg: Springer, 1978, pp.105–16
61. Leino AA, Lunttila T, Mozumder M, Pulkkinen A, Tarvainen T. Perturbation Monte Carlo method for quantitative photoacoustic tomography. *IEEE Trans Med Imaging* 2020;**39**:2985–95
62. Zangerl G, Moon S, Haltmeier M. Photoacoustic tomography with direction dependent data: an exact series reconstruction approach. *Inverse Probl* 2019;**35**:114005
63. Francis KJ, Arora A, Kancharla P, Singh MKA, Steenbergen W, Channappayya SS. Generative adversarial network-based photoacoustic image reconstruction from bandlimited and limited-view data. In: *SPIE international conference on photons plus ultrasound: imaging and sensing 1164235, (SPIE 2021)*, vol. 11642, 6–12 March 2021
64. Vu T, Li M, Humayun H, Zhou Y, Yao J. A generative adversarial network for artifact removal in photoacoustic computed tomography with a linear-array transducer. *Exp Biol Med* 2020;**245**:597–605
65. Sahlstrom T, Pulkkinen A, Tick J, Leskinen J, Tarvainen T. Modeling of errors due to uncertainties in ultrasound sensor locations in photoacoustic tomography. *IEEE Trans Med Imaging* 2020;**39**:2140–50
66. Kalva SK, Hui HH, Pramanik M. Calibrating reconstruction radius in a multi single-element ultrasound-transducer-based photoacoustic computed tomography system. *J Opt Soc Am* 2018;**35**:764–71

(Received September 13, 2021, Accepted January 24, 2022)